

# High-speed optical coherence tomography by circular interferometric ranging

Meena Siddiqui<sup>1,2,3</sup>, Ahhyun S. Nam<sup>2,4</sup>, Serhat Tozburun<sup>1,2,5</sup>, Norman Lippok<sup>1,2</sup>, Cedric Blatter<sup>1,2</sup> and Benjamin J. Vakoc<sup>1,2,3\*</sup>

**Existing three-dimensional optical imaging methods excel in controlled environments, but are difficult to deploy over large, irregular and dynamic fields. This means that they can be ill-suited for use in areas such as material inspection and medicine. To better address these applications, we developed methods in optical coherence tomography to efficiently interrogate sparse scattering fields, that is, those in which most locations (voxels) do not generate meaningful signal. Frequency comb sources are used to superimpose reflected signals from equispaced locations through optical subsampling. This results in circular ranging, and reduces the number of measurements required to interrogate large volumetric fields. As a result, signal acquisition barriers that have limited speed and field in optical coherence tomography are avoided. With a new ultrafast, time-stretched frequency comb laser design operating with 7.6 MHz to 18.9 MHz repetition rates, we achieved imaging of multi-cm<sup>3</sup> fields at up to 7.5 volumes per second.**

Most three-dimensional optical microscopies image across a fairly limited volumetric field and are difficult to apply to large samples<sup>1,2</sup>. This is particularly true when the samples have an irregular shape or when, due to sample motion, imaging must be performed rapidly. In medicine, for example, three-dimensional optical microscopies are rarely used to visualize surgical fields or to comprehensively image complex organs such as the bladder or colon. To better address these settings, wide-field and rapid three-dimensional imaging technologies are needed.

Optical coherence tomography (OCT) has scaled to image across large volumes in part because the method relies on coherent ranging rather than on beam focusing for depth sectioning<sup>3,4</sup>; recent works have demonstrated OCT imaging over expansive volumetric fields<sup>5–7</sup>. However, interrogating large volumes at high resolution implies measuring a large number of voxels. With current OCT approaches, this large voxel set can only be captured with a proportionally large set of measurements<sup>5–11</sup>. This in turn necessitates a massive signal acquisition bandwidth for high-speed imaging. It is now well appreciated that acquisition bandwidth is the key bottleneck in the development of rapid, large-volumetric-field OCT<sup>6–8</sup>.

Here, we present an interferometric ranging architecture, ‘circular coherent ranging’, that dramatically reduces (relative to Fourier domain (FD)-OCT) the number of measurements required to interrogate a large volumetric field, yet captures nearly identical measures of a sample’s three-dimensional structure. The key distinction lies in how each method handles sparsity. When imaging a large volumetric field, a significant portion of the field does not generate detectable scattering signals. This includes the regions above the sample surface (typically air) and beyond the penetration depth of light into the sample. Thus, the three-dimensionally resolved scattering measurements are often highly sparse. Existing FD-OCT uses a ranging architecture that independently measures each physical location (termed physical voxel), a method we refer to in this work as linear coherent ranging. As such, sparsity is replicated into the

measurement set. By contrast, circular ranging removes this sparsity from the measurement set by combining multiple physical voxels into each measured voxel<sup>12</sup>. The technique avoids a distortion of the sample’s three-dimensional structure through a circular mapping of physical delay/depth to measured delay/depth. Through the compression of the large physical voxel set into a reduced measured voxel set, imaging over a large volumetric field can be performed with substantially lower acquisition bandwidths.

## Results

Frequency comb sources provide the physical basis for circular ranging<sup>12,13</sup> (Fig. 1a). This contrasts with the continuous broadband sources typically utilized in linear coherent ranging. By using a frequency comb, signals from equidistant delays are combined optically. To illustrate this we present interferometric signals generated from linear and circular ranging approaches in Fig. 1a. In this example, three mirrors generate reflected signals with delays of  $\tau_0$ ,  $\tau_0 + \Delta\tau$ , and  $\tau_0 + 2\Delta\tau$ , all defined relative to a reference beam. An interference between the mirror reflections and the reference beam results in a sinusoidal spectral modulation. In linear ranging, the frequency of this modulation is directly proportional to delay; increasing delay results in a proportionally higher frequency<sup>14,15</sup>. In contrast, with a frequency comb, a finite and discrete set of equally spaced spectral lines ( $\nu_i = i\Delta\nu_{fc}$ , where  $i$  is an integer and  $\Delta\nu_{fc}$  is the comb free spectral range (FSR)) produces a low-frequency modulation<sup>12</sup> that is the same for all physical delays separated by  $\Delta\tau = 1/\Delta\nu_{fc}$  (Supplementary Information I). This maps multiple depth locations into a single interference fringe frequency.

For samples that generate scattering signals throughout the depth field, the superposition of multiple voxels would result in overlapping signals and lead to image artefacts. However, as described above, most long-range settings feature significant sparsity; elastic scattering signals begin at the sample surface, and are present to a finite sample depth (1–2 mm in most biological tissues).

<sup>1</sup>Harvard Medical School, Boston, MA, USA. <sup>2</sup>Wellman Center for Photomedicine, Massachusetts General Hospital, Boston, MA, USA. <sup>3</sup>Harvard-MIT Health Sciences & Technology (HST), Cambridge, MA, USA. <sup>4</sup>Department of Mechanical Engineering, Massachusetts Institute of Technology (MIT), Cambridge, MA, USA. Present address: <sup>5</sup>Izmir International Biomedicine and Genome Institute, Dokuz Eylul University, Balçova, Izmir, Turkey.

\*e-mail: [bvakoc@mgh.harvard.edu](mailto:bvakoc@mgh.harvard.edu)

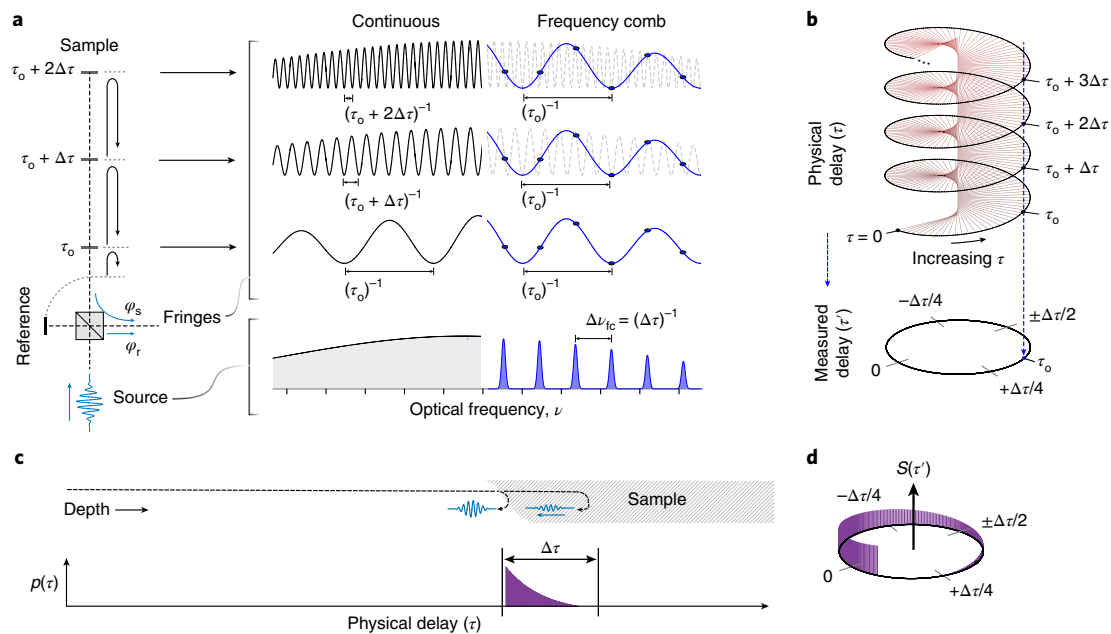


**Fig. 1 | Frequency comb circular ranging.** **a**, A ranging system measuring interference from three locations spaced equally by  $\Delta\tau$ . In FD-OCT measurements using a continuous broadband source (left), a spectral modulation is generated at a frequency that is proportional to the delay. Using a frequency comb source (right) with a comb spacing of  $\Delta\nu_{fc} = 1/\Delta\tau$ , each delay generates the same spectral modulation frequency, and this frequency is that associated with the base delay ( $\tau_0$ ). **b**, Circular mapping of physical delay to the measured delay space ( $\tau'$ ). Measured delays do not exceed  $|\Delta\tau/2|$  and have a total range  $\Delta\tau$ . **c**, The distributed scattering signal,  $p(\tau)$ , from a sample is depth-limited by attenuation in the sample. **d**, If the duration of the scattering signal in  $p(\tau)$  is less than  $\Delta\tau$ , then it can be measured without overlap in the compressed scattering signal,  $S(\tau')$ .

In these settings, extended depth ranges are used to accommodate the uncontrolled and/or dynamic position of the sample.

To capture these sparse, depth-confined signals without artefacts, we implement a circular mapping of the physical depth field to a reduced measurement space (Fig. 1b). To illustrate, Fig. 1c shows the scattering signal,  $p(\tau)$ , that results from a tissue sample located within a long depth/delay range. The signal is confined (by optical scattering and absorption) to the superficial tissue region (typically less than 2 mm). To profile this sample using linear ranging methods, the full delay range is interrogated, resulting in a measured scattering signal,  $s(\tau)$ , given by  $s(\tau) = p(\tau)$ . Circular ranging results in the direct measurement of a compressed scattering profile,  $S(\tau')$  (Fig. 1d), given as

$$S(\tau') = \sum_m p(\tau' + m\Delta\tau) \quad (1)$$

where  $\tau'$  is the circular (measured) delay,  $m$  is an integer,  $S(\tau')$  is measured from  $-\Delta\tau/2$  to  $+\Delta\tau/2$  and any scattering signal shorter in duration than  $\Delta\tau$  (or a circular depth range,  $\Delta d$ , given by  $\Delta d = c\Delta\tau/(2n)$  where  $c$  is the speed of light and  $n$  is the index of refraction) is mapped one-to-one and without overlap from any other signal within the circular delay space. This is achieved regardless of its position in physical space (Fig. 1d). In this way, these scattering profiles can be efficiently captured without control or a priori knowledge of the location of the sample. Note that the circular delay range ( $\Delta\tau$ ) and circular depth range ( $\Delta d$ ) are inversely related to the frequency comb spacing,  $\Delta\nu_{fc}$ . Hence,  $\Delta\nu_{fc}$  can be adjusted to fit the anticipated extent of the scattering signal. More generally, we note that  $\Delta d$  can be set to be less than the signal penetration depth. This is because reflected signals attenuate rapidly with depth in OCT, and thus superficial signals are negligibly affected by an overlap with the much smaller signals that originate from deeper locations. As such, the circular depth range  $\Delta d$  can be set to capture

the depth region of interest, even if that is smaller than the imaging penetration depth. The circular mapping described in Fig. 1b is achieved by performing complex fringe demodulation, that is, by detecting both in-phase ( $\sin[\varphi_s - \varphi_r]$ ) and quadrature ( $\cos[\varphi_s - \varphi_r]$ ) fringes (Supplementary Information I).

It is instructive to explicitly compare the imaging performance of linear and circular ranging methods. For both circular and linear ranging, the relationship between the measured voxel rate,  $V_m$ , and acquisition data bandwidth,  $B$ , is the same and given as

$$V_m < \frac{B}{2b} \quad (2)$$

where  $b$  is the bit depth of each measurement<sup>7</sup>. The methods differ in how the measured voxel rate relates to the physical voxel rate,  $V_p$ . For linear ranging,  $V_p = V_m$ . In circular ranging,  $C_f = \Delta z/\Delta d$  physical voxels are combined into each measured voxel, where  $\Delta z$  is the source coherence length (and both  $\Delta z$  and  $\Delta d$  are defined in air). As a result, the effective physical voxel measurement rate is given by  $V'_p = C_f V_m$ . For clarity, we use  $V'_p$  and  $V_p$  to denote physical voxel rates with and without compression, respectively. Thus, for a given acquisition data bandwidth, circular ranging supports the same measured voxel rate, but interrogates (although not independently) a physical voxel set that is larger by a factor of  $C_f$ . As an example, if we consider a practical continuous acquisition data bandwidth of  $B = 8$  gigabytes per second measured voxel rates cannot exceed  $V_m = 2$  gigavoxels per second (assuming  $b = 2$  bytes). A cubic-centimetre field comprising 2 physical gigavoxels could then be imaged at 1 volume per second using FD-OCT ( $V_p = V_m$ ). In circular ranging with a compression factor of  $C_f = 30$  (for example, assuming  $\Delta z = 3$  cm and  $\Delta d = 1$  mm), the same acquisition data bandwidth would allow 30 volumes per second ( $V'_p = C_f V_m$ ).

To realize these high voxel rates over centimetre-scale ranges, laser sources that have frequency comb spectra and sweep speeds

exceeding 10 MHz are needed. Because suitable sources did not exist, we developed a new time-stretched frequency comb laser source<sup>13</sup> based on active stretched-pulse mode-locking (SPML) principles<sup>16–18</sup>. A schematic of the laser is presented in Fig. 2, and additional details are provided in Supplementary Information II. In the laser cavity, an intensity modulator produces subnanosecond broadband optical pulses (position 1) that are repeated at a harmonic of the cavity round trip time. An intracavity Fabry–Perot (FP) etalon ( $\Delta\nu_{fc} = 200$  GHz) forces a frequency comb spectral structure in these pulses. Matched positive and negative dispersive fibres elastically stretch (position 2) and compress (position 3) the pulses from the modulator. In the stretched state, individual optical frequencies are separated to create a pulse train. This pulse train allows the spectral modulation to be measured rapidly in the time domain, avoiding the need for speed-limiting spectrometers. In addition to allowing serial measurement across optical frequency, the temporal separation of frequency comb lines also avoids gain competition in the semiconductor optical amplifier that would otherwise narrow the lasing bandwidth. We achieved 80 nm of optical bandwidth centred at 1,550 nm. Pulse separation (parameterized by  $\Delta t_{fc}$ ) was on the nanosecond scale and comb repetition rates of 18.9 MHz were achieved. An SPML laser configuration using a FP etalon with  $\Delta\nu_{fc} = 80$  GHz was also built and is described in Supplementary Fig. 5. The high finesse of the intracavity FP etalons created a narrow linewidth on each comb line, providing coherence-length-limited ranging depths that varied from 2 cm to 3.5 cm depending on the specific laser configuration.

Imaging was performed with the system design and microscope shown in Fig. 3a,b. In the constructed system, we implemented an all-optical polarization-based demodulation circuit to generate separate optical in-phase (I) and quadrature (Q) fringe signals as

previously described in ref. 19. These I/Q fringe signals were detected and digitized on separate channels. We also implemented (but not shown in Fig. 3) a second set of demodulation optical circuits and digitizers to achieve polarization-diverse detection (Supplementary Fig. 6). The radio frequency (RF) signals were low-pass filtered to remove out-of-band harmonics associated with the comb source. Signal processing to reconstruct circularly wrapped images follows described methods for FD-OCT<sup>4</sup> (Supplementary Information IV). A cone-beam microscope with a focusing lens located before the beam scanning mirrors was used for all imaging experiments; the specific details of the microscope for each experiment are detailed in Supplementary Table 1. As in FD-OCT, the source bandwidth determines depth resolution and the linewidth defines the source coherence length. The 80 nm bandwidth yielded a depth resolution of 14  $\mu\text{m}$  (in tissue,  $n = 1.38$ ). Unique to frequency comb circular ranging is the comb spacing parameter,  $\Delta\nu_{fc}$ , which sets the circular delay range,  $\Delta d$ . At 80 and 200 GHz line spacing, circular depth ranges were 1.358 mm and 543  $\mu\text{m}$  (in tissue) respectively.

To illustrate imaging by circular ranging, we employed the system to perform large-volume imaging across a human face (Fig. 3c–e). As in conventional OCT, cross-sectional (Fig. 3c,d) and en face (Fig. 3e) images are generated from the magnitude of the scattered signal plotted on a log scale. Unique to this work, these images are resolved across the circular rather than physical delay. A laser with  $\Delta\nu_{fc} = 200$  GHz and an 18.9 MHz repetition (that is, A-line) rate was used to capture signals across 543  $\mu\text{m}$  of depth in the tissue ( $\Delta d$ ). The circular delay wrapping nature of the scattering signal is clearly visible in the en face slices extracted from the compressed measurement set (Fig. 3e). Here, banding structures result from the summation of scattering signal from multiple equally spaced physical delays into each measured delay. An examination

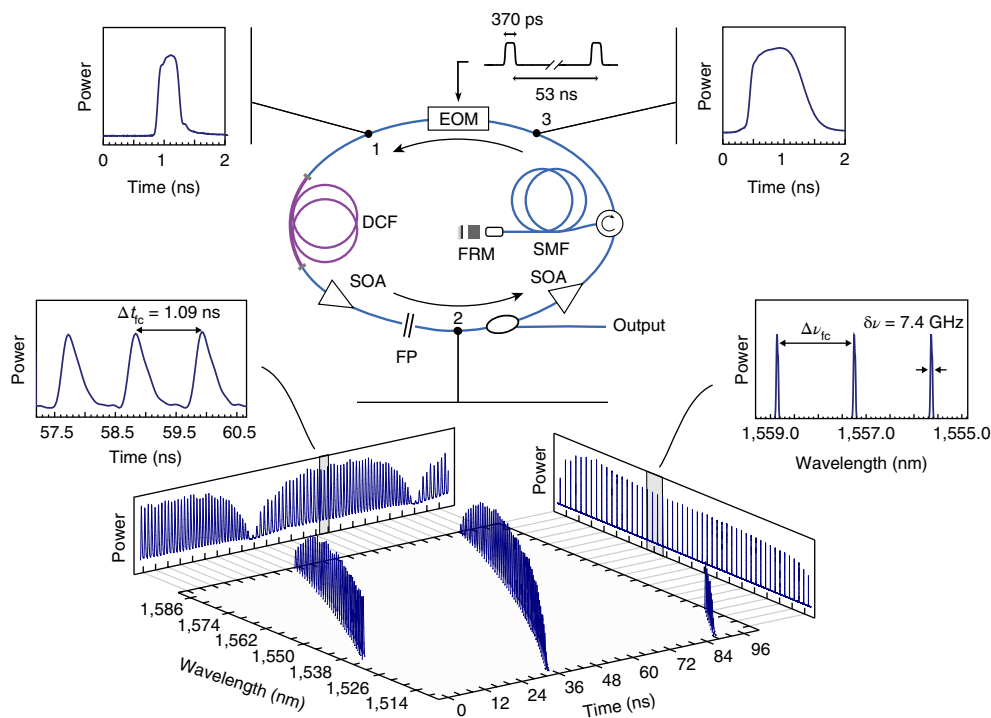


**Fig. 2 | A time-stretched frequency comb laser based on stretched-pulse mode-locking (SPML).** Broadband pulses of ~370 ps duration are generated by an electro-optic modulator (position 1), and are subsequently stretched (position 2) and compressed (position 3) by dispersive fibres. A spectral trace (lower 3D plot) shows comb-structured light with an overall bandwidth of 80 nm, comb separation of  $\Delta\nu_{fc} = 200$  GHz and linewidth of  $\delta\nu = 7.4$  GHz. In the stretched state, each optical frequency in the comb is separated in time by  $\Delta t_{fc} = 1.09$  ns. The repetition rate of the laser is ~18.9 MHz, a harmonic of the round-trip time of the cavity. DCF, dispersion compensating fibre; EOM, electro-optic modulator; FP, Fabry–Perot etalon; FRM, Faraday rotator mirror; SMF, single-mode fibre; SOA, semiconductor optical amplifier.

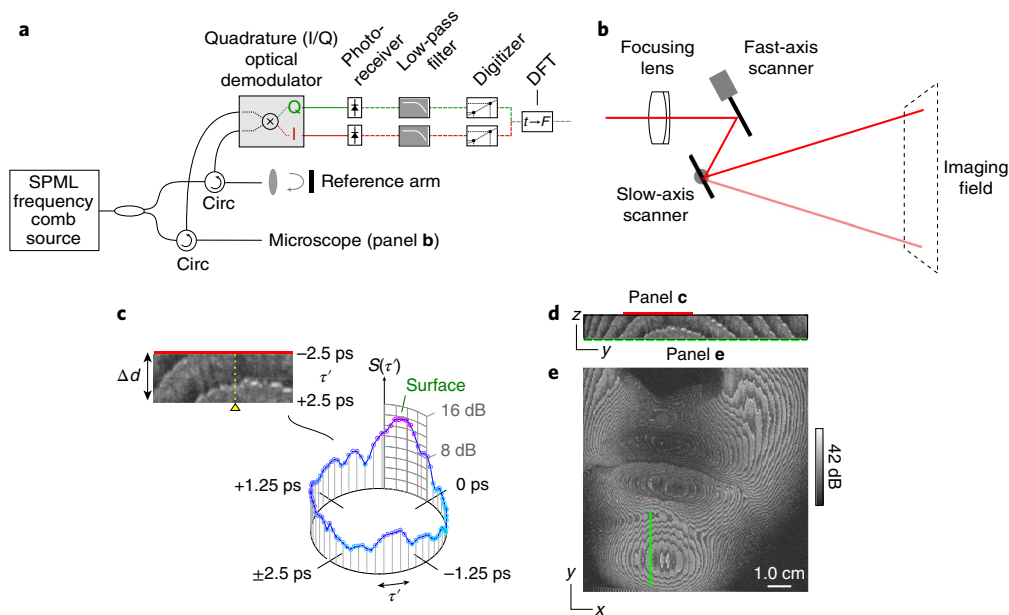


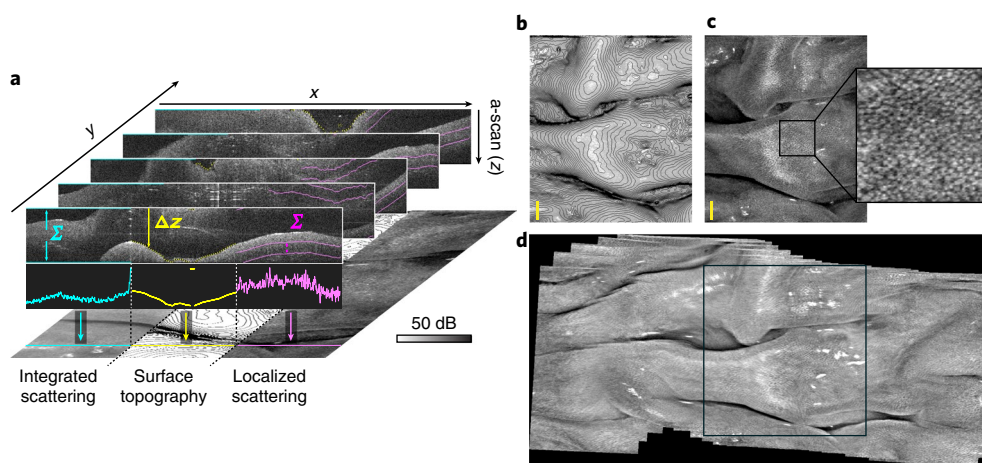
**Fig. 3 | Compressed optical coherence tomography system.** **a**, The interferometric and data capture system. Circ, optical circulator; DFT, discrete Fourier transform. **b**, The imaging microscope (parameters defined in Supplementary Information V). **c–e**, Wide-field three-dimensional imaging across a human face ( $9.5\text{ cm} \times 9.5\text{ cm}$  transverse field). **c**, A distributed scattering profile for a single transverse ( $xy$  space) location (denoted by the yellow dashed line) is shown. The signals are bounded from  $\tau' = -2.5\text{ ps}$  to  $+2.5\text{ ps}$ . Combining these depth profiles at adjacent transverse locations generates circularly wrapped cross-sectional images of subsurface structure (panel **c** inset and **d**). **e**, An en face slice (at  $\tau' = +1.29\text{ ps}$ ) of the full volumetric dataset from which the cross-sectional image of **d** was generated illustrates the superposition of signals generated at multiple equispaced physical delays. This superposition produces a banding pattern in the measured reflectivity at a given circular delay due to large variations in surface topography.

of the full three-dimensional dataset shows the comprehensive acquisition of all signals in the face (Supplementary Video 1). The coherence length of the source allowed capture of signals across a  $3.5\text{ cm}$  depth range in air ( $\Delta z$ ). This generated a compression factor of  $C_f = 47$  (calculated using  $\Delta d = 750\text{ }\mu\text{m}$  in air). With an axial resolution of  $14\text{ }\mu\text{m}$  in tissue ( $19.3\text{ }\mu\text{m}$  in air), an effective continuous physical voxel rate of  $V_p = 34$  gigavoxels per second ( $= 18.9\text{ MHz} \times 3.5\text{ cm} / 19.3\text{ }\mu\text{m}$ ) was achieved. This required an acquisition data bandwidth of only  $B = 3.68$  gigabytes per second (Supplementary Table 1). A more detailed discussion on the relationship between circular RF bandwidths and circular delays are presented in Supplementary Fig. 6.

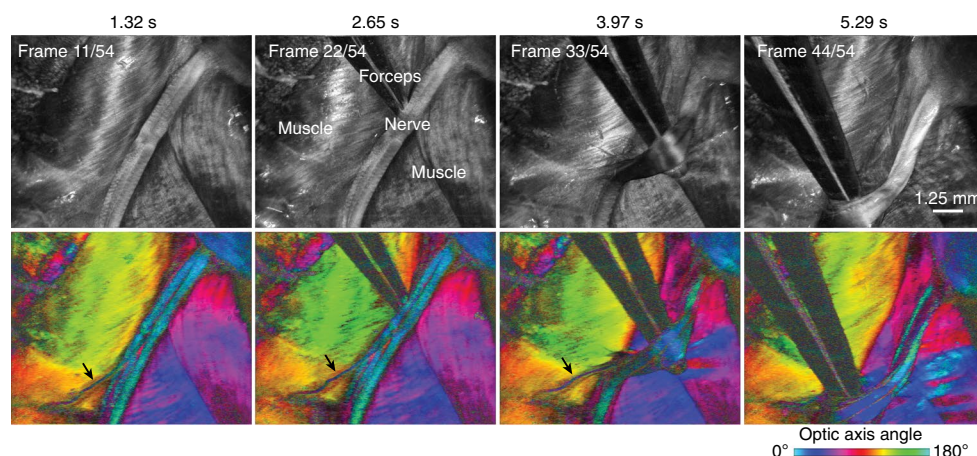
The ability to image continuously at these speeds and fields allows deployment to complex and dynamic environments. To demonstrate this capability, we present videos obtained by laterally scanning across ex vivo porcine colon with multi-centimetre tissue folds (Fig. 4 and Supplementary Video 2). The system was configured with  $\Delta\nu_c = 80\text{ GHz}$  ( $\Delta d = 1.358\text{ mm}$  in tissue), and provided a  $3\text{ cm}$  coherence-limited depth range ( $\Delta z$ ) at a  $7.59\text{ MHz}$  laser repetition rate. With an axial resolution of  $15.2\text{ }\mu\text{m}$  (in air), this yielded an effective  $V_p = 15$  gigavoxels per second ( $= 7.59\text{ MHz} \times 3\text{ cm} / 15.2\text{ }\mu\text{m}$ ) acquisition. The compression factor was  $C_f = 16$  (calculated using  $\Delta d = 1.87\text{ mm}$  in air). Volumetric images were acquired continuously at  $7.5$  volumes per second, yielding a four-dimensional dataset. To display this as a video, we generated several visualizations of the three-dimensional dataset. The blue (leftmost) panel in Fig. 4a illustrates a projection generated by averaging the log-scale reflectivities across the full circular depth range. The yellow (middle) panel in Fig. 4a shows topographic lines separated by  $50\text{ }\mu\text{m}$  derived using a surface finding algorithm. The magenta (rightmost) panel in Fig. 4a illustrates a projection generated by averaging the log-scale reflectivities across a localized depth range ( $200\text{--}400\text{ }\mu\text{m}$ ) relative to the surface. This last projection enhances crypt contrast relative to full depth range averaging. In the grey scale projections shown in

Fig. 4b–d, white denotes higher scattering. Both surface topography and crypt patterns could become key diagnostic features for early cancer screening<sup>20</sup>. In Fig. 4d, we employed frame-by-frame registration to create a mosaicked image, highlighting wide-field volumetric imaging by dynamic panning with rapid, continuous acquisition.

To demonstrate the flexibility of the approach, we implemented polarization-sensitive (PS) methods<sup>21</sup> to enable visualization of tissue birefringence. To perform PS measurements, we implemented intra-frame polarization modulation and derived birefringence using the Stokes formalism<sup>21,22</sup> (Supplementary Information IV). This system used a source configuration with  $\Delta\nu_c = 200\text{ GHz}$  ( $\Delta d = 543\text{ }\mu\text{m}$  in tissue), providing a  $2\text{ cm}$  coherence-limited depth range ( $\Delta z$ ) and an  $18.9\text{ MHz}$  depth-scan rate. Acquisition was performed with polarization diversity using four digitizer channels (I and Q on two polarization-channels; see Supplementary Fig. 7). The effective physical voxel imaging rate was  $V_p = 39.2$  gigavoxels per second across two polarization diverse channels ( $= 2 \times 18.9\text{ MHz} \times 2\text{ cm} / 19.3\text{ }\mu\text{m}$ ), and the compression factor was  $C_f = 27$  (calculated using  $\Delta d = 750\text{ }\mu\text{m}$  in air). We imaged a surgically exposed rat sciatic nerve with forcep manipulation at  $6.5$  volumes per second to mimic intra-surgical procedures (Fig. 5 and Supplementary Videos 3–5). Full circular depth range averaged log-scale intensity projections were performed as described in Fig. 4a to reveal subsurface microarchitectural features of the nerve (Fig. 5, top row)<sup>23,24</sup>. The polarimetric properties were analysed to extract the birefringence axis at each location. The angular orientation of this axis was mapped to a cyclic colour map, and median projections of the optic axis were generated across the full circular depth range to provide polarimetric tissue contrast (Fig. 5, bottom row). Of specific interest is the ability of these projections to highlight nerves with high contrast. This capability can be used to improve visualization of nerves underneath fascia or other tissues within a surgical field<sup>25</sup>. As in all video results, each frame of the video



**Fig. 4 | Rapid volumetric imaging of porcine colonic mucosa.** Imaging was performed with a field of  $1\text{ cm} \times 1.2\text{ cm}$ . **a**, An illustration of three algorithms used to extract three-dimensional features from a circular four-dimensional dataset. **b**, A single frame from Supplementary Video 2 of full-range-averaged log-scale intensity projection overlaid with topography data. **c**, A single frame and zoomed-in region from Supplementary Video 2 displaying depth-localized intensity. **d**, A wide-field image constructed by mosaicking the videos frames. The black rectangle denotes a single ( $1\text{ cm} \times 1.2\text{ cm}$ ) imaged field. Grey scale values in **b–d** highlight averaged log-scale signals; white denotes higher average scattering. Scale bars, 1.2 mm.



**Fig. 5 | Rapid volumetric imaging of a surgically exposed rat sciatic nerve with birefringence contrast.** Top: full range log-scale average intensity projection of an exposed rat sciatic nerve. White denotes higher averaged scattering. Bottom: polarization-sensitive display of birefringence axis. The birefringence axis is mapped to hue on a circular colour map, causing nerve/muscle tissues with different orientations to appear with distinct colours. The birefringence axis map reveals a small nerve not visible in structural imaging (black arrow). Four frames from a 8.3 s video acquisition are shown. During this acquisition, the nerve is manipulated with forceps. Real-time videos and cross-sectional fly-throughs can be viewed in Supplementary Videos 3–5.

is derived from a circularly wrapped three-dimensional dataset. Furthermore, from the PS measurements, parameters such as birefringence can be extracted to provide measures of nerve health (Supplementary Fig. 14 and Supplementary Video 6).

## Discussion

In summary, we have described a compressive coherent ranging method that enables new capabilities in rapid, continuous and large-volumetric-field OCT. The core photonic innovation—circular ranging with a frequency comb source that optically subsamples interference fringes—is an elegant solution to acquisition bandwidth barriers that limit OCT. With SPML frequency comb source architectures that support speeds up to 18.9 MHz, this technique allows near video-rate capture of cubic-centimetre fields. By implementing this subsampling in the optical (rather than the electronic) domain, the entire detection and acquisition system can operate at reduced bandwidths. Moreover, by reducing the measurement set

size, the technique reduces computational requirements for real-time generation of images from acquired signals.

In long-range OCT, there is a trade-off between transverse resolution and depth range (regardless of whether circular ranging or conventional Fourier-domain methods are used). However, even at centimetre-scale ranges, sufficient transverse resolutions can be achieved to support multiple imaging methods. For example, an OCT system operating at  $1.55\text{ }\mu\text{m}$  centre wavelength and employing Gaussian beams can achieve depths of focus from 0.5 cm to 3 cm with  $41\text{ }\mu\text{m}$  to  $101\text{ }\mu\text{m}$  transverse full-width at half-maximum (FWHM) resolutions. By transitioning to  $1.0\text{ }\mu\text{m}$  centre wavelengths, the same depths of focus can be achieved with resolutions from  $33\text{ }\mu\text{m}$  to  $81\text{ }\mu\text{m}$ . Many critical architectural features in biological samples and non-biological materials can be identified by structural OCT at these resolutions<sup>26–30</sup>. There are also multiple OCT contrast methods that are not based on resolving small structures, but instead measure broader properties of the tissue/materials. These include

attenuation coefficient imaging<sup>31,32</sup>, PS measures of birefringence, and spectroscopic methods<sup>33,34</sup> to characterize absorption and ultra-structure. In the future, methods that extend the depth of focus<sup>35–37</sup> (for example, by using Bessel beams) and/or autofocusing can be used to achieve higher transverse resolution imaging beyond the Gaussian diffraction limit. It is important to note that the circular ranging technique does not require a compromise in axial resolution. By preserving axial resolution, the influence of speckle noise can be reduced in spectroscopic, polarization-sensitive and attenuation coefficient imaging methods that analyse signals across depth.

**Code availability.** The spectral binning PS-OCT base code is available from the NIH-funded P41 Center for Biomedical OCT Research and Translation (CBORT) (<https://octresearch.org/resources/>).

**Data availability.** The data that support the plots within this paper are available from the corresponding author upon reasonable request.

Received: 13 March 2017; Accepted: 18 December 2017;  
Published online: 26 January 2018

## References

- Pawley, J. B. *Handbook of Biological Confocal Microscopy*. (Springer Science+ Business Media, New York, 20–42, 2006).
- Zipfel, W. R., Williams, R. M. & Webb, W. W. Nonlinear magic: multiphoton microscopy in biosciences. *Nat. Biotechnol.* **21**, 1369–1377 (2003).
- Huang, D. et al. Optical coherence tomography. *Science* **254**, 1178–1181 (1991).
- Drexler, W. et al. Optical coherence tomography today: speed, contrast, and multimodality. *J. Biomed. Opt.* **7**, 071412 (2014).
- Xu, J. et al. High-performance multi-megahertz optical coherence tomography based on amplified optical time-stretch. *Biomed. Opt. Express* **6**, 1340–1350 (2015).
- Wang, Z. et al. Cubic meter volume optical coherence tomography. *Optica* **3**, 1496–1503 (2016).
- Wieser, W. et al. High definition live 3D-OCT in vivo: design and evaluation of a 4D OCT engine with 1 GVoxel/s. *Biomed. Opt. Express* **5**, 2963–2977 (2014).
- Wieser, W., Biedermann, B. R., Klein, T., Eigenwillig, C. M. & Huber, R. Multi-megahertz OCT: high quality 3D imaging at 20 million A-scans and 4.5 GVoxels per second. *Opt. Express* **18**, 14685–14704 (2010).
- Song, S., Xu, J. & Wang, R. K. Long-range and wide field of view optical coherence tomography for in vivo 3D imaging of large volume object based on akinetic programmable swept source. *Biomed. Opt. Express* **7**, 4734–4748 (2016).
- Moon, S. & Kim, D. Y. Ultra-high-speed optical coherence tomography with a stretched pulse supercontinuum source. *Opt. Express* **14**, 11575–11584 (2006).
- Goda, K. et al. High-throughput optical coherence tomography at 800 nm. *Opt. Express* **20**, 19612–19617 (2012).
- Siddiqui, M. & Vakoc, B. J. Optical-domain subsampling for data efficient depth ranging in Fourier-domain optical coherence tomography. *Opt. Express* **20**, 17938–17951 (2012).
- Tozburun, S., Siddiqui, M. & Vakoc, B. J. A rapid, dispersion-based wavelength-stepped and wavelength-swept laser for optical coherence tomography. *Opt. Express* **22**, 3414–3424 (2014).
- Youngquist, R. C., Carr, S. & Davies, D. E. N. Optical coherence-domain reflectometry: a new optical evaluation technique. *Opt. Lett.* **12**, 158–160 (1987).
- Lexer, F., Hitzberger, C. K., Fercher, A. F. & Kulhavy, M. Wavelength-tuning interferometry of intraocular distance. *Appl. Opt.* **36**, 6548–6553 (1997).
- Tamura, K., Ippen, E. P., Haus, H. A. & Nelson, L. E. 77-fs pulse generation from a stretched-pulse mode-locked all-fiber ring laser. *Opt. Lett.* **18**, 1080–1082 (1993).
- Haus, H. A., Tamura, K., Nelson, L. E. & Ippen, E. P. Stretched-pulse additive pulse mode-locking in fiber ring laser: theory and experiment. *IEEE J. Quantum Electron.* **31**, 591–598 (1995).
- Lee, S., Kim, K. & Delfyett, P. J. eXtreme chirped pulse amplification-beyond the fundamental energy storage limit of semiconductor optical amplifiers. *IEEE Photon. Technol. Lett.* **18**, 799–801 (2006).
- Siddiqui, M., Tozburun, S., Zhang, E. Z. & Vakoc, B. J. Compensation of spectral and RF errors in swept-source OCT for high extinction complex demodulation. *Opt. Express* **23**, 5508–5520 (2015).
- Kudo, S. et al. Colonoscopic diagnosis and management of nonpolypoid early colorectal cancer. *World J. Surg.* **24**, 1081–1090 (2000).
- de Boer, J. F. & Milner, T. E. Review of polarization sensitive optical coherence tomography and Stokes vector determination. *J. Biomed. Opt.* **7**, 359–371 (2002).
- Villiger, M. et al. Spectral binning for mitigation of polarization mode dispersion artifacts in catheter-based optical frequency domain imaging. *Opt. Express* **21**, 16353–16369 (2013).
- Islam, M. S. et al. Extracting structural features of rat sciatic nerve using polarization-sensitive spectral domain optical coherence tomography. *J. Biomed. Opt.* **17**, 056012 (2012).
- Henry, F. P. et al. In vivo optical microscopy of peripheral nerve myelination with polarization sensitive optical coherence tomography. *J. Biomed. Opt.* **20**, 046002 (2015).
- Kitajima, K. et al. Visualization of periprostatic nerve fibers before and after radical prostatectomy using diffusion tensor magnetic resonance imaging with tractography. *Clin. Imaging* **38**, 302–306 (2014).
- Yun, S. E. et al. Comprehensive volumetric optical microscopy in vivo. *Nat. Med.* **12**, 1429–1433 (2006).
- Blatter, C., Meijer, E. F. J., Padera, T. P. & Vakoc, B. J. Simultaneous measurements of lymphatic vessel contraction, flow and valve dynamics in multiple lymphangions using optical coherence tomography. *J. Biophotonics* e201700017 (2017).
- Utku, B., Qin, W., Qi, X., Kalkan, G. & Wang, R. K. OCT-based label-free in vivo lymphangiography within human skin and areola. *Sci. Rep.* **6**, 1–8 (2016).
- Su, R. et al. Perspectives of mid-infrared optical coherence tomography for inspection and micrometrology of industrial ceramics. *Opt. Express* **22**, 15804–15819 (2014).
- Rong, S. et al. Optical coherence tomography for quality assessment of embedded microchannels in alumina ceramic. *Opt. Express* **20**, 4603–4618 (2012).
- Yuan, W., Kut, C., Liang, W. & Li, X. Robust and fast characterization of OCT-based optical attenuation using a novel frequency-domain algorithm for brain cancer detection. *Sci. Rep.* **7**, 1–8 (2017).
- Vermeer, K. A., Mo, J., Weda, J. J. A., Lemij, H. G. & de Boer, J. F. Depth-resolved model-based reconstruction of attenuation coefficients in optical coherence tomography. *Biomed. Opt. Express* **5**, 322–337 (2013).
- Fleming, C. P., Eckert, J., Halpern, E. F., Gardecki, J. A. & Tearney, G. J. Depth resolved detection of lipid using spectroscopic optical coherence tomography. *Biomed. Opt. Express* **4**, 1269–1284 (2013).
- Leitgeb, R. et al. Spectral measurement of absorption by spectroscopic frequency-domain optical coherence tomography. *Opt. Lett.* **25**, 820–822 (2000).
- Lorenser, D., Singe, C. C., Curatolo, A. & Sampson, D. D. Energy-efficient low-Fresnel-number Bessel beams and their application in optical coherence tomography. *Opt. Lett.* **39**, 548–551 (2014).
- Lee, K. S. & Rolland, J. P. Bessel beam spectral-domain high-resolution optical coherence tomography with micro-optic axicon providing extended focusing range. *Opt. Lett.* **33**, 1696–1698 (2008).
- Liao, W. et al. Endoscopic optical coherence tomography with a focus-adjustable probe. *Opt. Lett.* **42**, 4040–4043 (2017).

## Acknowledgements

This research was sponsored by the National Institutes of Health (NIH) grants R01CA163528, P41EB015903 and DOD/AFOSR FA9550-11-1-0331, Harvard Medical School Bullock Post-Doctoral Fellowship, and the National Science Foundation (NSF) Graduate Research Fellowships Program (11-031). Additional financial support provided by Alcon. The authors thank I. Chico-Calero for performing animal surgeries and M. Villiger for providing the spectral binning PS-OCT base code.

## Author contributions

M.S. built the system, planned and executed experiments, performed image processing, and prepared the manuscript. A.S.N. contributed to polarization-sensitive signal processing. S.T. contributed to building the system. N.L. executed experiments and contributed to image processing. C.B. was involved in developing the system software. B.J.V. obtained support, managed the project and participated in manuscript preparation.

## Competing interests

The authors are inventors on intellectual property owned by the Massachusetts General Hospital.

## Additional information

**Supplementary information** is available for this paper at <https://doi.org/10.1038/s41566-017-0088-x>.

**Reprints and permissions information** is available at [www.nature.com/reprints](http://www.nature.com/reprints).

**Correspondence and requests for materials** should be addressed to B.J.V.

**Publisher's note:** Springer Nature remains neutral with regard to jurisdictional claims in published maps and institutional affiliations.